Chinese Chemical Letters 37 (2026) 112125

Contents lists available at ScienceDirect

Chinese Chemical Letters

journal homepage: www.elsevier.com/locate/cclet

Regulation of catalytic efficiency and enantioselectivity for supramolecular chiral polyaniline@Pt-Ni$_x$ nanocomposites as nanozymes *via* tunable alloy composition

Chu Wang[a,b], Zheng Xi[a,*], Rufang Zhao[c,*], Xiaohuan Sun[a], Jie Han[a,*], Rong Guo[a]

[a] *Jiangsu Provincial Key Laboratory of Green & Functional Materials and Environmental Chemistry, College of Chemistry and Materials, Yangzhou University, Yangzhou 225002, China*
[b] *School of Chemistry and Materials Science, Jiangsu Normal University, Xuzhou 221116, China*
[c] *Hubei Key Laboratory of Pollutant Analysis & Reuse Technology, College of Chemistry and Chemical Engineering, Hubei Normal University, Huangshi 435002, China*

ARTICLE INFO

Article history:
Received 11 May 2025
Revised 1 November 2025
Accepted 16 November 2025
Available online 17 November 2025

Keywords:
Supramolecular chirality
Nanozymes
Platinum-nickel nanoparticles
Polyaniline
Enantioselective catalysis

ABSTRACT

Nanozymes have demonstrated significant potential as robust enzyme-mimicking catalysts due to their high stability, low cost and easy preparation. However, achieving precise enantioselective control of nanozymes remains a significant challenge. In this study, the supramolecular chiral nanozymes were engineered by integrating supramolecular chiral polyaniline (*P*/*M*-PANI) scaffolds with platinum-nickel nanoparticles (Pt-Nix NPs). The resulting *P*/*M*-PANI@Pt-Nix nanozymes exhibited high catalytic activity toward the oxidation of 3,4-dihydroxy-*S*/*R*-phenylalanine (*S*/*R*-DOPA). Moreover, systematic modulation of the Pt/Ni atomic ratio in Pt-Nix NPs enabled precise regulation of interfacial interactions and chiral transfer effects, thereby optimizing enantioselectivity. Density functional theory (DFT) calculations further revealed that the distinct adsorption energies of DOPA and its oxidation products on Pt-Nix surfaces directly correlated with the observed catalytic efficiency trends. This work demonstrated that compositional tuning of catalytic centers is an effective strategy for manipulating both catalytic efficiency and enantioselectivity, providing valuable insights for the rational design of smart supramolecular chiral nanozymes.

© 2026 Published by Elsevier B.V. on behalf of Chinese Chemical Society and Institute of Materia Medica, Chinese Academy of Medical Sciences.

Nanozymes, as enzyme-mimicking nanomaterials, have emerged as attractive alternatives to natural enzymes due to their high stability, low cost and easy preparation [1–5]. Though extensive studies have focused on enhancing the catalytic efficiency of nanozymes, their enantioselective capabilities remain largely underexplored [6–8]. Moreover, precise enantioselective control in nanozymes presents a significant challenge due to their predominantly achiral nature [9–11].

Among various strategies to construct chiral nanozymes, integrating supramolecular chiral architectures with catalytic centers has been proven to be highly effective [12–14]. In this context, polyaniline (PANI)-based supramolecular scaffolds have drawn considerable attention because of their superior chemical stability and versatile supramolecular assembly properties [15–18]. The PANI supramolecular chiral scaffolds have been employed in combination with catalytic centers including Fe_3O_4, Au and transition metal ions (*e.g.*, Cu^{2+}, Zn^{2+}) to construct chiral nanozymes capable of enantioselective catalysis of 3,4-dihydroxy-*S*/*R*-phenylalanine (*S*/*R*-DOPA) [19–21]. Nevertheless, current research on PANI-based supramolecular chiral nanozymes primarily focuses on improving their enantioselective performance. To the best of our knowledge, regulating catalytic efficiency and enantioselectivity through compositional control have not been reported yet, but it is essential for the comprehensive understanding of chirality transfer effects and the origin of enantioselectivity. Among various nanozymes, alloy nanoparticles, such as platinum-nickel nanoparticles (Pt-Ni$_x$ NPs), have garnered significant attention due to their superior catalytic activity, which stems from their small size, high surface area and abundant active sites [22–24]. Previous studies have demonstrated that precise compositional tuning of these nanoparticles can effectively modulate their geometric and electronic structures, thereby optimizing their catalytic performance [25,26].

Herein, we engineered a series of supramolecular chiral nanozymes, *P*/*M*-PANI@Pt-Ni$_x$ (where x represents the Pt/Ni atomic

* Corresponding authors.
E-mail addresses: xizheng@yzu.edu.cn (Z. Xi), zhaorf@hbnu.edu.cn (R. Zhao), hanjie@yzu.edu.cn (J. Han).

https://doi.org/10.1016/j.cclet.2025.112125
1001-8417/© 2026 Published by Elsevier B.V. on behalf of Chinese Chemical Society and Institute of Materia Medica, Chinese Academy of Medical Sciences.

ratio of Pt-Ni_x NPs), by integrating supramolecular chiral scaffolds (*P*/*M*-PANI) with Pt-Ni_x NPs. The resulting *P*-PANI@Pt-Ni_x nanozymes exhibited remarkable enantioselective catalytic activity toward *S*-DOPA oxidation, while *M*-PANI@Pt-Ni_x nanozymes preferentially catalyzed the oxidation of *R*-DOPA. Furthermore, systematic adjustment of the Pt/Ni atomic ratio effectively modulated the interface interactions and chiral transfer effects between the *P*/*M*-PANI scaffolds and the Pt-Ni_x NPs, thereby enabling precise control over enantioselectivity. Density functional theory (DFT) calculations further revealed the distinct adsorption behaviors of DOPA and its oxidation products on various Pt-Ni_x interfaces, providing mechanistic insights into the observed differences in catalytic efficiency of *P*/*M*-PANI@Pt-Ni_x nanozymes. This study, for the first time, demonstrated that tailoring the composition of the catalytic center can simultaneously regulate both catalytic efficiency and enantioselectivity, offering an innovative strategy for the controllable design of supramolecular chiral nanozymes.

In a typical synthesis procedure, equimolar amounts of Pt(II) acetylacetonate and Ni(II) acetylacetonate were co-reduced in benzyl ether, which functioned as the reaction medium and reducing agent. Oleic acid, oleylamine and tetradecanediol were employed as surface stabilizers. To render the resulting nanoparticles hydrophilic, a ligand exchange process was performed using 3,4-dihydroxyphenylacetic acid. Inductively coupled plasma atomic emission spectrometry (ICP-AES) analysis indicated the atomic ratio of Pt to Ni in the resulting Pt-Ni NPs is ~1:1, consistent with the stoichiometric ratio of the Pt/Ni precursors introduced during the synthesis (Table S1 in Supporting information). In addition, nanoparticles with different Pt/Ni atomic ratios, specifically Pt-$Ni_{0.5}$ NPs and Pt-Ni_2 NPs, were synthesized by adjusting the precursor ratios. ICP-AES analysis further confirmed that the atomic ratios of Pt-$Ni_{0.5}$ NPs and Pt-Ni_2 NPs closely matched the intended molar ratios of the Pt/Ni precursors.

As demonstrated by the transmission electron microscopy (TEM) images, Pt-$Ni_{0.5}$ NPs, Pt-Ni NPs and Pt-Ni_2 NPs all exhibited *quasi*-spherical morphologies with average diameters of approximately 8 nm (Figs. 1a-c, Fig. S1 in Supporting information). X-ray diffraction (XRD) patterns revealed that these nanoparticles possess a face-centered cubic (*fcc*) crystal structure, characterized by the distinct (111) diffraction peak (Fig. S2 in Supporting information). Furthermore, the (111) diffraction peak position of Pt-Ni_x NPs lies intermediate between pure Pt (39.8°) and pure Ni (44.5°), providing clear evidence for successful alloy formation [27,28]. The high-resolution transmission electron microscopy (HRTEM) images of the Pt-Ni NPs clearly revealed lattice fringes with an interplanar spacing of 0.25 nm, which corresponded to the (111) crystal plane of the *fcc* structure (Fig. 1d).

Subsequently, based on previous reports, the polymerization of aniline was carried out using (*S*/*R*)-camphor-10-sulfonic acid (*S*/*R*-CSA) as the chiral inducing agent, leading to the formation of the *P*/*M*-PANI-CSA precursor [29]. As shown in Figs. S3a and b (Supporting information), the *P*-PANI-CSA prepared with *S*-CSA exhibited a right-handed twist, while *R*-CSA induced the left-handed helical structure. Furthermore, the chiral structure of *P*/*M*-PANI-CSA was verified by ultraviolet-visible (UV-vis) and circular dichroism (CD) spectroscopy (Fig. S4 in Supporting information), with mirror imaged Cotton effects were observed in the CD spectra. The obtained *P*/*M*-PANI-CSA were subjected to a stepwise secondary doping process involving ammonia solution and thioglycolic acid, yielding the *P*/*M*-PANI supramolecular chiral scaffolds. Due to the molecular memory effect, the helical structure of *P*/*M*-PANI remained well-preserved after CSA removal (Figs. S3c and d in Supporting information). Finally, successful fabrication of *P*/*M*-PANI@Pt-Ni_x nanocomposites was achieved through the integration of synthesized Pt-Ni_x NPs with the *P*/*M*-PANI supramolecular chiral scaffolds. TEM and scanning electron microscopy (SEM) images displayed the uniform distribution of Pt-Ni_x NPs on the *P*/*M*-PANI surface, while the characteristic helical morphology was effectively retained (Figs. 1e-g, Fig. S5 in Supporting information). In addition, XRD analysis revealed characteristic diffraction peaks corresponding to both *P*-PANI and Pt-Ni_x NPs in *P*-PANI@Pt-Ni_x (Fig. S6 in Supporting information). High-angle annular dark field scanning transmission electron microscopy (HAADF-STEM) imaging combined with energy-dispersive X-ray spectroscopy (EDS) elemental mapping analysis of C, N, O, S, Ni and Pt in *P*-PANI@Pt-Ni further demonstrated the successful integration of Pt-Ni NPs with the *P*/*M*-PANI scaffolds (Figs. 1h-n).

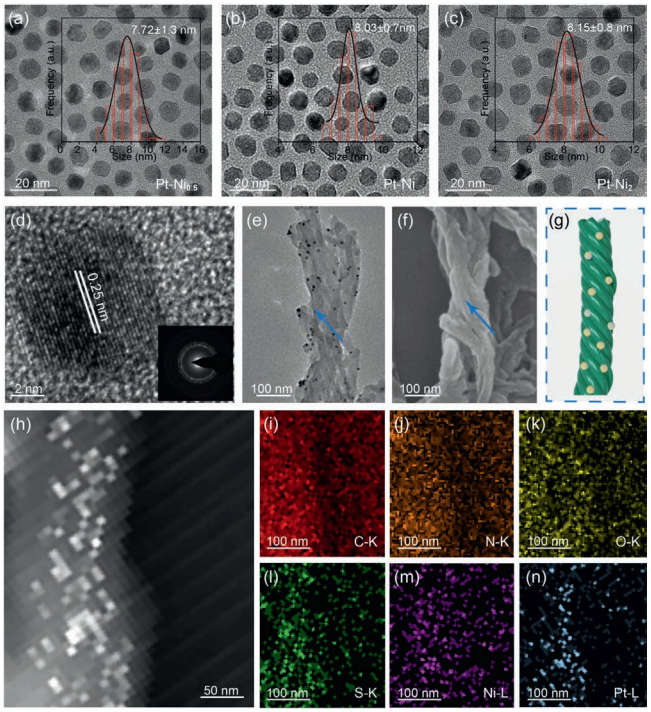


Fig. 1. TEM images and size distribution histograms (inset) of (a) Pt-$Ni_{0.5}$ NPs, (b) Pt-Ni NPs and (c) Pt-Ni_2 NPs. (d) HRTEM image of the Pt-Ni NPs. (e) TEM, (f) SEM and (g) model images of *M*-PANI@Pt-Ni. (h) HAADF-STEM image for *P*-PANI@Pt-Ni. The EDS mapping of (i) C, (j) N, (k) O, (l) S, (m) Ni and (n) Pt for *P*-PANI@Pt-Ni.

To further clarify the chiroptical properties of the nanocomposites, the UV-vis and CD spectra were measured (Fig. 2a).

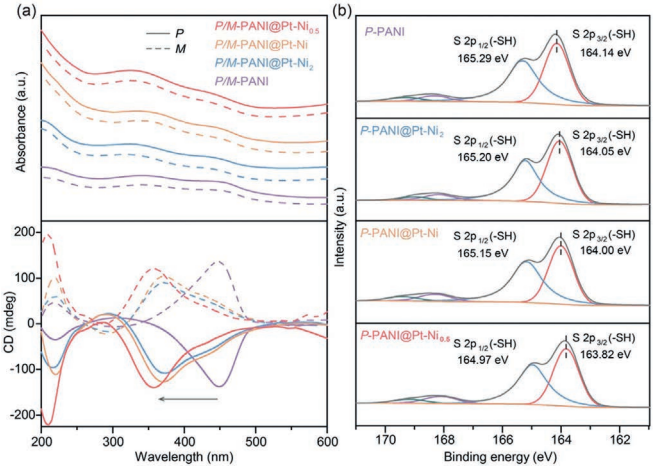


Fig. 2. (a) UV-vis and CD spectra for *P*/*M*-PANI, *P*/*M*-PANI@Pt-Ni_2, *P*/*M*-PANI@Pt-Ni and *P*/*M*-PANI@Pt-$Ni_{0.5}$. (b) XPS spectra of S 2p for *P*-PANI, *P*-PANI@Pt-Ni_2, *P*-PANI@Pt-Ni and *P*-PANI@Pt-$Ni_{0.5}$.

The UV-vis spectra indicated that *P*/*M*-PANI@Pt-Ni_2, *P*/*M*-PANI@Pt-Ni and *P*/*M*-PANI@Pt-$Ni_{0.5}$ nanocomposites exhibited significantly enhanced absorption at 330 nm compared to *P*/*M*-PANI, which can be attributed to the successful integration of the *P*/*M*-PANI supramolecular chiral scaffolds with Pt-Ni_x NPs. As shown in CD spectra, no signals were observed in the 200-600 nm wavelength range for Pt-Ni_x NPs, indicating their achiral characteristics (Fig. S7a in Supporting information). Moreover, the strong opposite CD peaks at 450 nm were observed for *P*-PANI and *M*-PANI, confirming their distinct chiral environments. Upon the incorporation of Pt-Ni_x NPs, new peaks at 350 nm appeared of all these *P*/*M*-PANI@Pt-Ni_x nanocomposites. It is noteworthy that the CD spectra of *P*/*M*-PANI@Pt-Ni and *P*/*M*-PANI@Pt-Ni_2 featured a prominent peak at 350 nm alongside a smaller peak at 450 nm. In contrast, the *P*/*M*-PANI@Pt-$Ni_{0.5}$ predominantly exhibited a pronounced peak at 350 nm, with the original 450 nm signal nearly diminished. The CD peak intensities at 350 nm decreased in the order of *P*/*M*-PANI@Pt-$Ni_{0.5}$ > *P*/*M*-PANI@Pt-Ni > *P*/*M*-PANI@Pt-Ni_2, indicating strongest chiral transfer effect between *P*/*M*-PANI scaffolds and Pt-$Ni_{0.5}$ NPs. Moreover, considering that Pt-$Ni_{0.5}$ NPs exhibited a characteristic absorption at 260 nm (Fig. S7b in Supporting information), the appearance of a new CD peak at 260 nm in *P*/*M*-PANI@Pt-$Ni_{0.5}$ suggests successful chiral transfer from the *P*/*M*-PANI supramolecular scaffolds to Pt-$Ni_{0.5}$ NPs. Additionally, high-resolution X-ray photoelectron spectroscopy (XPS) spectra of S 2p was obtained to further reveal the interface interactions. As indicated in Fig. 2b, the binding energy of S $2p_{3/2}$ (-SH) in *P*/*M*-PANI@Pt-Ni_x nanocomposites showed a noticeable negative shift compared with sole *P*-PANI (164.14 eV), which clearly indicated a strong interface interaction between PANI and Pt-Ni_x NPs. Notably, the most pronounced negative shift was observed for *P*-PANI@Pt-$Ni_{0.5}$, with the binding energy of S $2p_{3/2}$ (-SH) decreasing to 163.82 eV. Moreover, as revealed in Fig. S8a (Supporting information), the XPS spectra of Pt 4f demonstrated that Pt species on the surface of Pt-Ni_x NPs primarily exist in the metallic Pt(0) state. Meanwhile, the XPS analysis of Ni 2p also revealed the compositional variations among the different Pt-Ni_x NPs (Fig. S8b in Supporting information). Based on above-mentioned results, it is safe to say that a series of *P*/*M*-PANI@Pt-Ni_x nanocomposites with chiral environment were successfully constructed.

Chiral molecules are widely recognized for their crucial roles in biological systems. A notable example is the differential biological activities of DOPA enantiomers: *S*-DOPA is clinically effective in treating Parkinson's disease, whereas its enantiomer *R*-DOPA exhibits toxicity in humans [9]. Thus, the enantioselective catalytic capability of *P*/*M*-PANI@Pt-Ni_x nanocomposites was evaluated using *S*/*R*-DOPA as the model substrate. The reaction kinetics were followed by measuring the UV-vis absorption at 475 nm, corresponding to the formation of dopachrome, the distinctive oxidation product of DOPA. As illustrated in Fig. S9 (Supporting information), all *P*-PANI@Pt-Ni_x nanozymes exhibited significantly higher catalytic efficiency toward *S*-DOPA than *R*-DOPA. In contrast, the *M*-PANI@Pt-Ni_x nanozymes displayed superior catalytic efficiency for *R*-DOPA. To further quantify the catalytic efficiency and enantioselectivity of the synthesized *P*/*M*-PANI@Pt-Ni_x nanozymes, steady-state kinetic assays were conducted. The typical Michaelis-Menten kinetics, determined by measuring initial reaction rates as a function of *S*/*R*-DOPA concentrations, are illustrated in Figs. 3a-f. It is evident that the *P*-PANI@Pt-Ni_x preferentially catalyzed *S*-DOPA, whereas all *M*-PANI@Pt-Ni_x showed the catalytic selectivity toward *R*-DOPA.

The enzymatic kinetic parameters, specifically the turnover number (k_{cat}) and the Michaelis constant (K_m), were derived from the Michaelis-Menten curves and are summarized in Tables S2 and S3 (Supporting information). Meanwhile, the overall catalytic efficiency, expressed as the ratio k_{cat}/K_m, was calculated and presented in Fig. 3g. Notably, the catalytic efficiency (k_{cat}/K_m) of *P*/*M*-PANI@Pt-Ni_x nanozymes exhibited a positive correlation with the Ni content in the surface-loaded Pt-Ni_x NPs, which is consistent with the analysis of k_{cat}. Among these nanozymes, *P*/*M*-PANI@Pt-Ni_2 exhibited the highest catalytic efficiency, while *P*/*M*-PANI@Pt-$Ni_{0.5}$ displayed the lowest. This trend can be primarily attributed to differences in the intrinsic catalytic activity of various Pt-Ni_x NPs. To further evaluate the enantioselective performance of these nanozymes, the select factor, expressed as the ratio of k_{cat}/K_m toward *S*- and *R*-DOPA enantiomers (>1), was calculated. *P*-PANI@Pt-$Ni_{0.5}$ and *M*-PANI@Pt-$Ni_{0.5}$ achieved the highest select factors of 2.15 and 2.26 (Fig. 3h), outperforming most reported chiral nanozymes (Table S4 in Supporting information). In addition, the select factors of *P*/*M*-PANI@Pt-Ni_x increased in the order of *P*/*M*-PANI@Pt-Ni_2 < *P*/*M*-PANI@Pt-Ni < *P*/*M*-PANI@Pt-$Ni_{0.5}$, a trend that strongly correlated with the degree of chiral transfer and the strength of interface interactions. The activation energy (E_a) was determined by linear regression analysis of the logarithmic reaction rate versus the inverse reaction temperature, following the Arrhenius equation (Fig. 3i, Figs. S10 and S11 in Supporting information). The E_a for *S*/*R*-DOPA oxidation catalyzed by *P*/*M*-PANI@Pt-Ni_x nanozymes were consistently lower compared to those for *R*/*S*-DOPA oxidation, providing additional evidence for the enantioselective catalytic behavior. It is noteworthy that *P*/*M*-PANI@Pt-Ni_2 exhibited the lowest E_a for DOPA oxidation among these nanozymes, which is consistent with their highest catalytic efficiency.

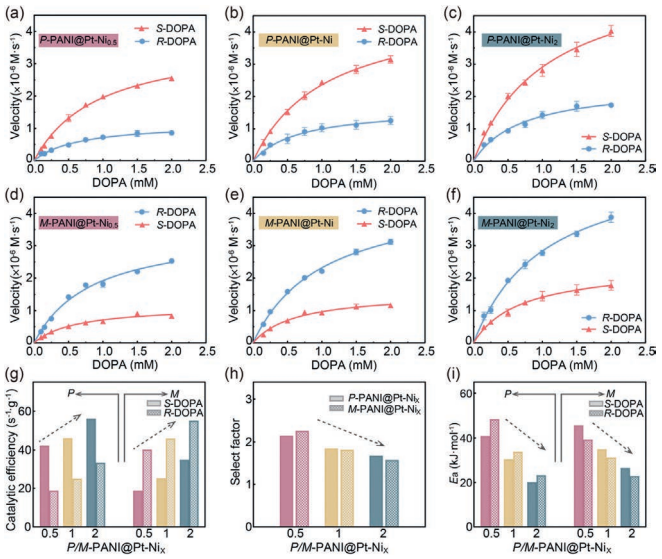


Fig. 3. Michaelis-Menten curves for (a, d) *P*/*M*-PANI@Pt-$Ni_{0.5}$, (b, e) *P*/*M*-PANI@Pt-Ni and (c, f) *P*/*M*-PANI@Pt-Ni_2 catalyzing *S*/*R*-DOPA. The histograms of (g) catalytic efficiency, (h) select factor and (i) E_a for *P*/*M*-PANI@Pt-Ni_x catalyzing *S*/*R*-DOPA.

As discussed above, the differences in catalytic efficiency among these nanozymes are likely associated with the intrinsic catalytic performance of catalytic centers loaded on the *P*/*M*-PANI surface. However, direct evidence elucidating the underlying mechanisms responsible for these variations remains limited. To further elucidate the origin of the excellent catalytic efficiency of Pt-Ni_2 NPs, DFT calculations were performed to investigate the oxidation of DOPA across different Pt-Ni_x surfaces. Three (111) slab models were constructed, each including four alloy layers of (i) Pt-$Ni_{0.5}$ (Pt/Ni = 2:1), (ii) Pt-Ni (Pt/Ni = 1:1) and (iii) Pt-Ni_2 (Pt/Ni = 1:2) to represent the catalytic surfaces of Pt-$Ni_{0.5}$ NPs, Pt-Ni NPs and Pt-Ni_2 NPs, respectively. Subsequently, the adsorption behaviors of DOPA and dopachrome on these catalytic surfaces were simulated. The adsorption energies of DOPA and dopachrome were cal-

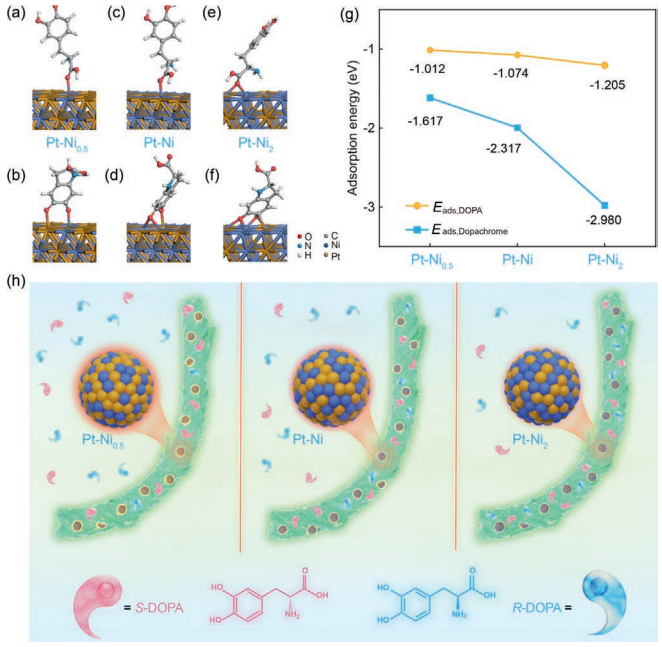


Fig. 4. Optimal absorption behaviors of (a, c, e) DOPA and (b, d, f) dopachrome on the (a, b) Pt-$Ni_{0.5}$, (c, d) Pt-Ni and (e, f) Pt-Ni_2 model catalytic surfaces. (g) Adsorption energies for DOPA and dopachrome on the Pt-$Ni_{0.5}$, Pt-Ni and Pt-Ni_2 model catalytic surfaces in (a-f). (h) Schematic illustration of the enantioselective catalytic performance of *P*/*M*-PANI@Pt-Ni_x.

culated and employed as key descriptors to assess the adsorption strength. All possible adsorption configurations are presented in Figs. S12-S17 (Supporting information), with the most stable adsorption configurations summarized in Figs. 4a-f. Among the three catalytic surfaces, Pt-Ni_2 exhibited the lowest adsorption energies for both DOPA and dopachrome, with values of -1.205 eV and -2.980 eV, respectively. In contrast, Pt-$Ni_{0.5}$ showed the highest adsorption energies for DOPA (-1.012 eV) and dopachrome (-1.617 eV). As illustrated in Fig. 4g, the adsorption energies of DOPA and dopachrome decreased with decreasing Pt/Ni atomic ratio on the catalytic surface. These results provide a clear explanation for the observed trend in catalytic efficiency among these nanozymes: *P*/*M*-PANI@Pt-Ni_2 > *P*/*M*-PANI@Pt-Ni > *P*/*M*-PANI@Pt-$Ni_{0.5}$.

Moreover, the distinct enantioselectivity observed in *P*/*M*-PANI@Pt-$Ni_{0.5}$, *P*/*M*-PANI@Pt-Ni and *P*/*M*-PANI@Pt-Ni_2 nanozymes can be attributed to the varying degrees of chiral transfer between *P*/*M*-PANI scaffolds and Pt-Ni_x NPs with different Pt/Ni atom ratios. To gain deeper insights into the origins of the catalytic performance differences observed in *P*/*M*-PANI@Pt-Ni_x nanozymes, enantioselective adsorption experiments were conducted using *P*-PANI@Pt-Ni_x as the representative nanozymes. Following 4h incubation of *P*-PANI@Pt-Ni_x nanozymes with the racemic solution of DOPA, the filtrate was subjected to CD and UV-vis measurements. As displayed in Fig. S18 (Supporting information), the CD and UV-vis spectra revealed that *P*-PANI@Pt-$Ni_{0.5}$ exhibited the weakest adsorption toward DOPA, yet displayed the highest enantioselectivity. In contrast, *P*-PANI@Pt-Ni_2 demonstrated the strongest DOPA adsorption capacity but the lowest enantioselectivity. As illustrated in Fig. 4h, this enantioselective adsorption behavior resulting in reduced catalytic efficiency but enhanced enantioselective performance for *P*-PANI@Pt-$Ni_{0.5}$, while *P*-PANI@Pt-Ni_2 exhibited superior catalytic efficiency and diminished enantioselectivity.

In conclusion, this study successfully developed a series of supramolecular chiral nanozymes, *P*/*M*-P@Pt-Ni_x, that integrate *P*/*M*-PANI supramolecular chiral scaffolds with Pt-Ni_x NPs. These nanozymes demonstrated significant enantioselectivity in the catalytic oxidation of *S*/*R*-DOPA. Moreover, the interface interaction and the chiral transfer effects were effectively modulated by tuning the composition of Pt-Ni_x NPs, enabling precise control over the enantioselectivity of the nanozymes. In addition, DFT calculations provided crucial insights into the mechanistic origins of the observed variations in catalytic efficiency among different nanozymes. This study not only established an innovative approach for the systematic design of chiral nanozymes but also highlighted the pivotal role of compositional tuning in optimizing catalytic performance. The findings offered essential guidelines for fabricating advanced supramolecular chiral nanozymes with tailored properties, demonstrating significant potential for applications in biocatalysis.

CRediT authorship contribution statement

Chu Wang: Writing – original draft, Visualization, Methodology, Investigation, Formal analysis, Data curation. **Zheng Xi:** Writing – review & editing, Supervision, Methodology, Funding acquisition, Conceptualization. **Rufang Zhao:** Writing – original draft, Methodology, Investigation. **Xiaohuan Sun:** Methodology, Conceptualization. **Jie Han:** Writing – review & editing, Supervision, Funding acquisition, Conceptualization. **Rong Guo:** Supervision, Conceptualization.

Declaration of competing interest

The authors declare that they have no known competing financial interests or personal relationships that could have appeared to influence the work reported in this paper.

Acknowledgments

This work was supported by the National Natural Science Foundation of China (Nos. 22572166, 22202171, 21922202 and 22272146), the Natural Science Foundation of Jiangsu Basic Research Program (No. BK20220559), the Jiangsu Specially-Appointed Professor Plan (Z. X.) from the Jiangsu Education Department, and the Postgraduate Research&Practice Innovation Program of Jiangsu Province (Yangzhou University) (No. KYCX23_3504).

Supplementary materials

Supplementary material associated with this article can be found, in the online version, at doi:10.1016/j.cclet.2025.112125.

References

[1] J. Wu, X. Wang, Q. Wang, et al., Chem. Soc. Rev. 48 (2019) 1004–1076.
[2] L. Jiao, H. Yan, Y. Wu, et al., Angew. Chem. Int. Ed. 59 (2019) 2565–2576.
[3] Y. Huang, J. Ren, X. Qu, Chem. Rev. 119 (2019) 4357–4412.
[4] S. Singh, Front. Chem. 7 (2019) 46.
[5] M. Zandieh, J.W. Liu, Adv. Mater. 36 (2024) 202211041.
[6] J.P. Richard, Biochemistry 52 (2013) 2009–2011.
[7] Y. Li, J. Liu, Mater. Horiz. 8 (2021) 336-350.
[8] H. Fan, R. Zhang, K. Fan, et al., ACS Nano 18 (2024) 2533–2540.
[9] Y. Zhou, Y. Wei, J.S. Ren, et al., Mater. Horiz. 7 (2020) 3291–3297.
[10] M. Sha, L. Rao, W. Xu, et al., Nano Lett. 23 (2023) 701–709.
[11] Y. Zhou, W. Wei, F. Cui, et al., Chem. Sci. 11 (2020) 11344–11350.
[12] C. Wang, Z. Xi, X. Sun, et al., Chem. Commun. 60 (2024) 14798–14801.
[13] D. Li, C. Gao, C. Zhao, et al., Chem. Commun. 60 (2024) 4569–4572.
[14] S. Song, J. Wang, N. Song, et al., Nanoscale 12 (2020) 2422–2433.
[15] M.R. Majidi, L.A. Kane-Maguire, G.G. Wallace, Polymer 36 (1995) 3597–3599.
[16] L.A. Kane-Maguire, A.G. Macdiarmid, I.D. Norris, et al., Synth. Met. 106 (1999) 171–176.
[17] H. Goto, J. Polym. Sci, A: Polym. Chem. 45 (2007) 2085–2090.
[18] X. Sun, Q. Ye, J. Zhou, et al., Chem. Synth. 3 (2023) 16.
[19] C. Wang, G. Yuan, C. Wang, et al., Small Struct. 4 (2023) 2200405.
[20] G. Yuan, Z. Xi, C. Wang, et al., Acta Phys. Chim. Sin. 39 (2023) 2212061.
[21] G. Yuan, C. Wang, Z. Xi, et al., Small 19 (2023) 202303739.
[22] X. Wang, G. Wei, W. Liu, et al., Anal. Chem. 95 (2023) 5937–5945.
[23] Z. Xi, K. Wei, Q. Wang, et al., J. Am. Chem. Soc. 143 (2021) 2660–2664.

[24] J.G. You, Y.W. Liu, C.Y. Lu, et al., Biosens. Bioelectron. 92 (2017) 442–448.
[25] X. Shen, W. Liu, X. Gao, et al., J. Am. Chem. Soc. 137 (2015) 15882–15891.
[26] W. Guo, M. Zhang, Z. Lou, et al., ChemCatChem 11 (2018) 737–743.
[27] V.R. Stamenkovic, B. Fowler, B.S. Mun, et al., Science 315 (2007) 493–497.
[28] C. Chen, Y.J. Kang, Z.Y. Huo, et al., Science 343 (2014) 1339–1343.
[29] W.G. Li, H.L. Wang, J. Am. Chem. Soc. 126 (2004) 2278–2279.